Robotica (2016) volume 34, pp. 1151–1167. © Cambridge University Press 2014
doi:10.1017/S0263574714002112

Dimensional optimization of the Stewart platform based on inertia decoupling characteristic

Zhihua Liu, Xiaoqiang Tang*, Zhufeng Shao and Liping Wang

Department of Mechanical Engineering, The State Key Laboratory of Tribology, Tsinghua University, Beijing 100084, China

(Accepted July 16, 2014. First published online: August 8, 2014)

SUMMARY

Inertia strongly influences the dynamic performance of parallel manipulators, and ignorance of inertia is apt to result in negative phenomena such as vibrations, overshoot, and slow response. This study analyzes the inertia-decoupling characteristic of Stewart platform. Because the inertia matrix of the Stewart platform is usually non-diagonal, inertia coupling occurs between its legs. Herein, decoupling to inertia is implemented, and independent control channels are determined. The influence of decoupled inertia on the control system is analyzed using the Adams simulation software, and the inertia index of the Stewart platform is proposed. Experiments are conducted on a prototype of the Stewart platform to verify the eigenvalue characteristic of decoupled inertia. The distribution of inertia index in the operational workspace is provided, and the influence of dimensional parameters on inertia index is discussed. Finally, dimensional optimization is realized with a set of optimized dimensions for good dynamic performance.

KEYWORDS: Inertia matrix, Decoupling, Eigenvalue, Parallel manipulator.

1. Introduction

Parallel manipulators possess potential advantages in terms of load-carrying capacity and dynamic performance,[1] and have wide applications in machine tools,[2,3] positioning devices,[4,5] and motion simulators.[6,7] Inertia strongly influences dynamic performance, especially in the case of parallel manipulators with requirements of high speed and heavy load. Ignorance of inertia is apt to result in negative phenomena such as vibrations, overshoot, and slow response. Research on the inertia of parallel manipulators is necessary to provide theoretical support for servomotor selection and dimensional design.

Inverse dynamic modeling of parallel manipulators is the foundation for inertia research. Based on different mechanical principles, several methods exist for establishing a dynamic model such as the Newton–Euler method,[8] the Lagrange formulation,[9] the principle of virtual work,[10] the Kane method,[11] and the generalized momentum approach.[12] In general, inverse dynamic formulations fall into one of the two categories: joint space dynamics and task space dynamics. Since the driving forces of a parallel manipulator are generated by servomotors mounted on the legs, the joint space inverse dynamic equation describes the relationship between the forces and accelerations of drivers at a given configuration and is adopted in the present paper to analyze inertia.

Inertia strongly influences the control strategy of a parallel manipulator. The control strategies of parallel manipulators can be largely divided into two schemes: task space control[13,14] and joint space control.[15–19] Joint space control is a type of tracking control for following the desired leg length computed by inverse kinematics. Numerous joint space control strategies have been proposed by researchers, including PD control with gravity compensation,[15] robust tracking control,[16] nonlinear PID control,[17] adaptive control,[18] and fuzzy sliding mode control.[19] However, the classical PID

* Corresponding author. E-mail: tang-xq@mail.tsinghua.edu.cn

https://doi.org/10.1017/S0263574714002112 Published online by Cambridge University Press

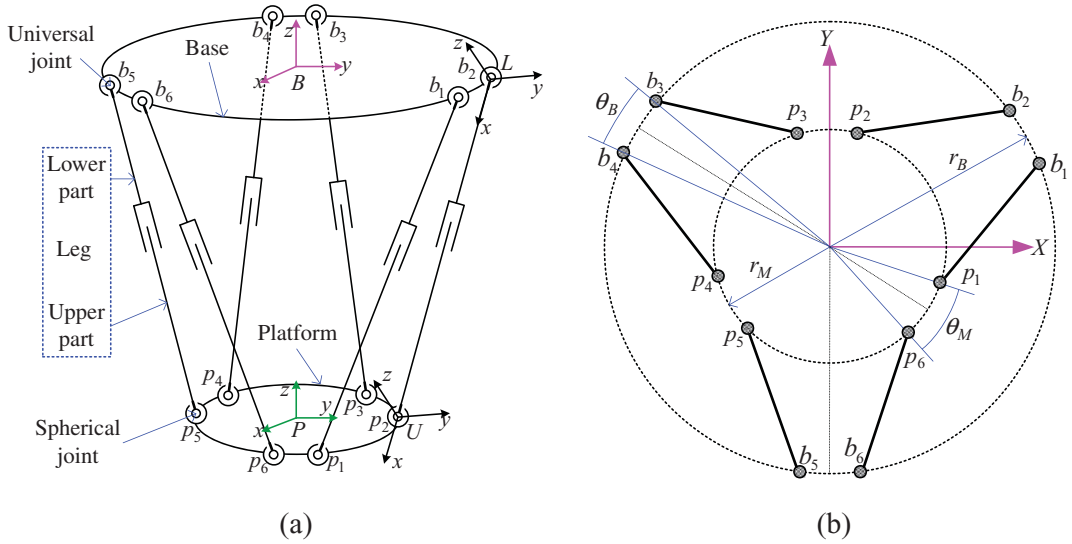


Fig. 1. The Stewart platform.

control, which offers the advantages of simplicity and reliability, is widely employed in industry. To achieve good dynamic performance, inertia is a key factor in adjusting the PID parameters.

The inertia problem of parallel manipulators has been studied by few researchers. Huang *et al.*[20] estimated the maximum inertia using the inertia matrix for servomotor selection. Chen and McInroy[21] proposed decoupled control of flexure-jointed hexapods using an estimated joint space inertia matrix. However, inertia coupling exists between freedoms of a parallel manipulator because of its nonlinear structural characteristics. Shao *et al.*[22,23] proposed the practical inertia matching principles for parallel manipulators that consider mechanical resonance frequency, acceleration torque, and dynamic performance. Ogbobe *et al.*[24] presented an analysis of coupling effects between degrees of freedom based on the singular value decomposition of inertia matrix. Yao *et al.*[25] investigated the block diagonal dominance property of inertia matrix. The previous studies have primarily focused on coupling inertia matrix. In order to fully understand the inertia of a parallel manipulator, research on inertia decoupling of a parallel manipulator is critically needed to put forward inertia index. The inertia index is very important in servomotor selection, control-parameter tuning, and dimensional optimization. In this paper, dimensional optimization based on the proposed inertia index of the Stewart platform is realized for good dynamic performance.

The study object of this paper is a 6-UPS Stewart platform. This paper is organized as follows: In Section 2, we implement decoupling to inertia of the Stewart platform. In Section 3, the decoupled inertia is analyzed using the Adams simulation software, and the inertia index of the Stewart platform is proposed. In Section 4, experiments designed to verify the theory proposed in this paper are discussed. In Section 5, applications of inertia index are presented, including the distribution of inertia index, the influence of dimensional parameters, and the optimization of dimensional parameters. Finally, the conclusions of the present paper are given.

2. Inertia Decoupling

As shown in Fig. 1, the Stewart platform comprises a base, a platform, and six legs. Each leg is connected to the base by a universal joint b_i and to the platform by a spherical joint p_i. The universal joints b_i ($i = 1 \ldots 6$) are distributed in a circle of radius r_B, and the angle of two adjacent points is θ_B. The spherical joints b_i ($i = 1 \ldots 6$) are distributed in a circle of radius r_M, and the angle of two adjacent points is θ_M.

The coordinates are set up as follows. Let $\{B\}$ be the base frame, with its origin at the geometric center of the base, the y-axis crossing the midpoint of b_2b_3, and the z-axis perpendicular to the base platform plane. Let $\{L\}$ be the lower part of the leg frame, with its origin at b_i, its x-axis along the leg, and its y-axis along the fixed pivot of the universal joint. Let $\{U\}$ be the upper part of the leg

https://doi.org/10.1017/S0263574714002112 Published online by Cambridge University Press

frame, with its origin at p_i, parallel to the local frame $\{L\}$. Let $\{P\}$ be the platform frame, with its origin at the geometric center of the platform, the y-axis crossing the midpoint of p_2p_3, and the z-axis perpendicular to the platform plane.

The dynamic equation of the Stewart platform in joint space[8] is

$$\mathbf{H}^{-1}\mathbf{I}_t\mathbf{H}^{-T}\ddot{\mathbf{L}} + \mathbf{H}^{-1}\left(\eta - \mathbf{J}\mathbf{H}^{-T}\mathbf{u}\right) = \mathbf{F} + \mathbf{H}^{-1}\begin{bmatrix}\Re\mathbf{F}_{\text{ext}}\\ \Re\mathbf{M}_{\text{ext}}\end{bmatrix}, \tag{1}$$

where $\mathbf{H}$ is the input–output force transformation matrix; $\mathbf{I}_t$ is the combined inertia of the leg and platform; $\ddot{\mathbf{L}}$ is the acceleration of legs; η is the force due to gravity, Coriolis acceleration, and viscous friction at joints; $\mathbf{u}$ is the centripetal acceleration of the connection point of the platform and leg; $\mathbf{F}$ is the driving force of actuators; $\mathbf{F}_{\text{ext}}$ and $\mathbf{M}_{\text{ext}}$ are external forces and moments acting on the platform; and $\Re$ is the rotation matrix specifying the orientation of the platform and is explained in detail in Appendix A.

According to Eq. (1), we can obtain the equivalent inertia matrix converted to motor shaft as

$$\mathbf{I} = \left(\frac{d}{2\pi}\right)^2 \mathbf{H}^{-1}\mathbf{I}_t\mathbf{H}^{-T}, \tag{2}$$

where d is the lead of the screw.

The dynamic model of motors can be expressed as:

$$\mathbf{T} = \mathbf{I}\ddot{\boldsymbol{\alpha}} + \mathbf{J}_m\ddot{\boldsymbol{\alpha}}, \tag{3}$$

where $\mathbf{T} = [T_1, T_2, T_3, T_4, T_5, T_6]^T$ is the motor torque, $\mathbf{J}_m = \text{diag}\,(J_m, J_m, \ldots, J_m)$ is the moment of inertia of motors and screws, and $\ddot{\boldsymbol{\alpha}} = [\alpha_1, \alpha_2, \alpha_3, \alpha_4, \alpha_5, \alpha_6]^T$ is the angular acceleration of motors.

The simulation model of Eq. (3) is depicted in Fig. 2. Non-diagonal element I_{ij} of the inertia matrix $\mathbf{I}$ describes coupling effects between the ith motor and the jth motor. The inertia problem of the Stewart platform is very complicated because a coupling effect exists between any two motors of the Stewart platform.

In parallel manipulators, the inertia matrix $\mathbf{I}$ is configuration-dependent and real symmetric. At a given configuration, simultaneous diagonalization of the real symmetric matrix $\mathbf{I}$ is given as

$$\mathbf{P}^{-1}\mathbf{I}\mathbf{P} = \boldsymbol{\Lambda}, \tag{4}$$

where $\mathbf{P}$ is an orthogonal matrix, $\boldsymbol{\Lambda} = \text{diag}\,(\lambda_1, \lambda_2, \ldots, \lambda_6)$ is a diagonal matrix, and $\lambda_1 \le \lambda_2 \le \lambda_3 \le \lambda_4 \le \lambda_5 \le \lambda_6$ are eigenvalues.

Taking the left product of Eq. (3) with $\mathbf{P}^{-1}$, we get:

$$\overline{\mathbf{T}} = \boldsymbol{\Lambda}\ddot{\overline{\boldsymbol{\alpha}}} + \mathbf{J}_m\ddot{\overline{\boldsymbol{\alpha}}}, \tag{5}$$

where $\overline{\mathbf{T}} = \mathbf{P}^{-1}\mathbf{T}$ and $\ddot{\overline{\boldsymbol{\alpha}}} = \mathbf{P}^{-1}\ddot{\boldsymbol{\alpha}}$.

The dynamic model of inertia decoupling of motors is expressed in Eq. (5). Its simulation model is presented in Fig. 3. Mapping from $\overline{\mathbf{T}}$ to $\ddot{\overline{\boldsymbol{\alpha}}}$ is regarded as a dynamic model of six virtual motors. Each motor is individual, and no inertia coupling occurs between motors. The eigenvalue λ_i is the load inertia of the ith virtual motor.

So far, joint space PID control for the Stewart platform is widely employed in industry. As shown in Fig. 4, we performed inverse kinematics to convert task space desired trajectory $\mathbf{x}$ to the desired leg length $\mathbf{L}$ and to individually control each leg to follow its desired length $\mathbf{L}$. Usually, the PID controller consists of a position loop, a speed loop, and a current loop. Similarly, simulation model of the inertia decoupling of the Stewart platform based on the joint PID control is illustrated in Fig. 5, where **In** is motors' positional command for the PID controller, **Out** is motors' actual position, G_P is the position controller, G_V is the speed controller, G_I is the current controller, L is armature winding inductance, R_a is armature winding resistance, K_t is the motor torque constant, and K_E is the back-ElectroMotive Force (EMF) constant.

https://doi.org/10.1017/S0263574714002112 Published online by Cambridge University Press

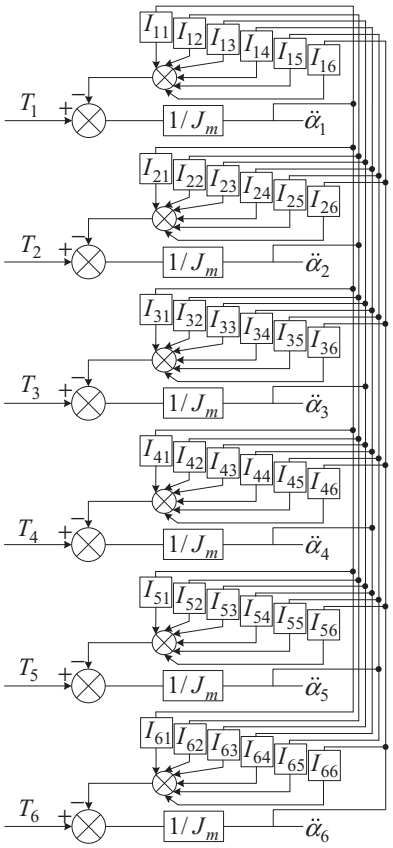


Fig. 2. Simulation model of motors.

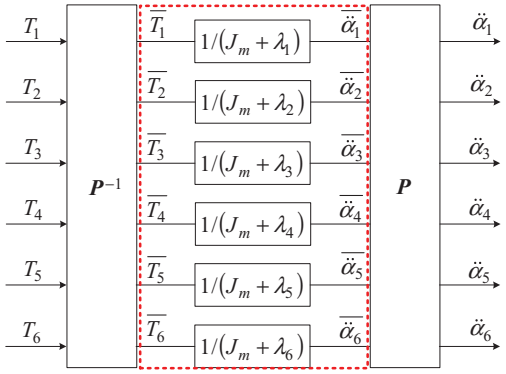


Fig. 3. Inertia decoupling of motors.

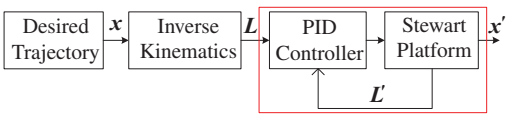


Fig. 4. Joint space PID control strategy.

Control channels from command signal $\overline{\mathbf{In}}$ to output signal $\overline{\mathbf{Out}}$ inside the red box in Fig. 5 are independent of each other. The eigenvalue λ_i of the inertia matrix $\mathbf{I}$ turns out to be the load inertia of the ith control channel. Inertia decoupling of the Stewart platform based on the joint space PID control is achieved. At a given configuration of the Stewart platform, the command signal $\overline{\mathbf{In}}$ is obtained by taking the left product of the positional command $\mathbf{In}$ with the simultaneous matrix $\mathbf{P}^{-1}$, and the actual

https://doi.org/10.1017/S0263574714002112 Published online by Cambridge University Press

Table I. Simulation parameters.

Symbol	Physical meaning	Value
L	Armature winding inductance	0.0144 H
R	Armature winding resistance	7.12 Ω
J_M	Motor inertia	1.64×10^{-5}kg · m^2
K_E	Back-EMF constant	0.405 V·s/rad
K_t	Motor torque constant	0.45 N·m/A
K_{pi}	Scale factor of current loop	18 V/A
T_{ii}	Integral time constant of current loop	0.002 s
K_{pv}	Scale factor of speed loop	0.06 A·s/rad
T_{iv}	Integral time constant of speed loop	0.001 s
K_{pp}	Scale factor of position loop	50 s^{-1}
d	Lead of the screw	5 mm

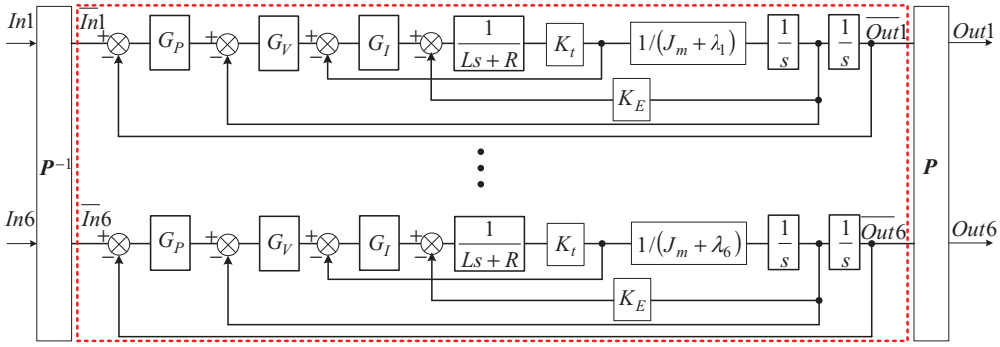


Fig. 5. Inertia decoupling of the Stewart platform.

position **Out** is obtained by taking the left product of the output signal $\overline{\mathbf{Out}}$ with the simultaneous matrix **P**.

3. Inertia Index

The relationship between the positional command **In** and the actual position **Out** can be expressed as

$$\mathbf{Out} = \mathbf{P}\text{diag}\,(H_1, H_2, \ldots, H_6)\,\mathbf{P}^{-1}\mathbf{In}, \tag{6}$$

where $H_i = \frac{\overline{\text{Out}i}}{\text{In}i}$ is the transfer function of the ith channel with the load inertia λ_i.

According to Eq. (6), the ratio of the ith actual position to the jth positional command $\frac{\text{Out}i}{\text{In}j}$ is the linear superposition of H_1, H_2,..., H_6. Thus, H_1, H_2,..., H_6 are regarded as six fundamental transfer functions. The simultaneous matrix can be expressed in terms of eigenvectors as $\mathbf{P} = [\mathbf{P}_1, \mathbf{P}_2, \ldots, \mathbf{P}_6]$. If the positional command vector coincides with the ith eigenvector as $\mathbf{In} = k\mathbf{P}_i$, according to Eq. (6) the actual position is $\mathbf{Out} = kH_i\mathbf{P}_i$. In this case, all control channels have the same transfer function H_i, which means that the six motors bear the same load inertia of the corresponding eigenvalue λ_i.

In the following section, the Adams simulation will be implemented to analyze the decoupled inertia. The Adams model of the Stewart platform is established as shown in Fig. 6. Control systems of the motors are established with Controls Toolkit in Adams, as shown in Fig. 7. Input blocks of the control system are the angle, the angular velocity, and the angular acceleration of the motor. The parameters of the Adams model are given in Appendix A, and the parameters of the control system are listed in Table I. A large scale factor of position loop K_{pp} is selected to clear the dynamic performance of the position tracking of the control system. At a configuration of $[0,0,-1.037\text{m},0^\circ,0^\circ,0^\circ]^T$, the maximum and minimum eigenvalues, along with their corresponding

https://doi.org/10.1017/S0263574714002112 Published online by Cambridge University Press

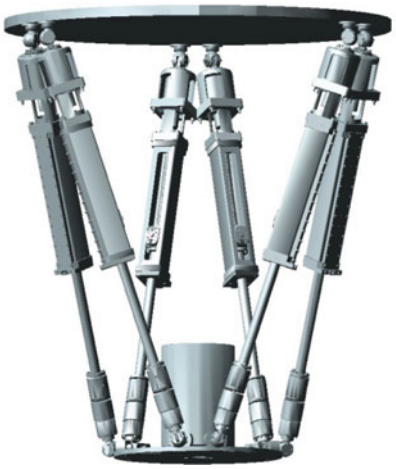


Fig. 6. Adams model.

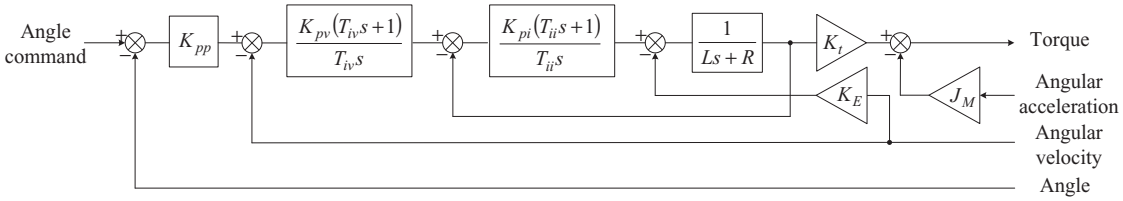


Fig. 7. Control system of motor.

eigenvectors, are calculated according to Eqs. (2) and (4) respectively:

$$\lambda_1 = 0.50 \times 10^{-5}, \quad \mathbf{P}_1 = [-0.4774, -0.3943, -0.0425, 0.5624, 0.5199, -0.1681]^T,$$
$$\lambda_6 = 19.15 \times 10^{-5}, \quad \mathbf{P}_6 = [-0.3347, -0.4133, 0.5748, -0.1425, -0.2400, 0.5558]^T.$$

To highlight the influence of inertia on the driving force, small motional ranges of motors are adopted in the simulation according to Eq. (1). On the other hand, the eigenvalues and the corresponding eigenvector change little because of the small motional ranges. The motors are desired to track sinusoidal signals with a frequency of 2π Hz and an amplitude of $\frac{\pi}{2}\mathbf{P}_i$ rad. The responses of motors to minimum and maximum eigenvalues are shown in Fig. 8.

As shown in Fig. 8(b), considerable vibration appears in the position tracking of motors, and the vibration trends of the six motors are the same. This poor dynamic performance of motors results from the large load inertia equaling maximum eigenvalue. In contrast, the dynamic performance depicted in Fig. 8(a) is better. In this case, the motors are running with the load inertia of minimum eigenvalue. The plots of driving forces required in the six legs to track the desired command signals are shown in Fig. 8(c) and (d). It is seen that the driving forces of maximum eigenvalue are much greater than the forces of minimum eigenvalue. The substantially diverging driving forces of maximum eigenvalue result from the high frequency vibration in the position tracking of motors. The results clearly show that the load inertia converted to motor shaft depends on the direction of the positional command. The eigenvalues of the inertia matrix prove to be the load inertia of control channels. These results reflect the influence of inertia on the control system of the Stewart platform because the mechanical structure in the simulation is an ideal model whose stiffness is infinite. For the sake of driving forces, too large maximum eigenvalue of inertia matrix should be avoided in case of vibration of the control system.

https://doi.org/10.1017/S0263574714002112 Published online by Cambridge University Press

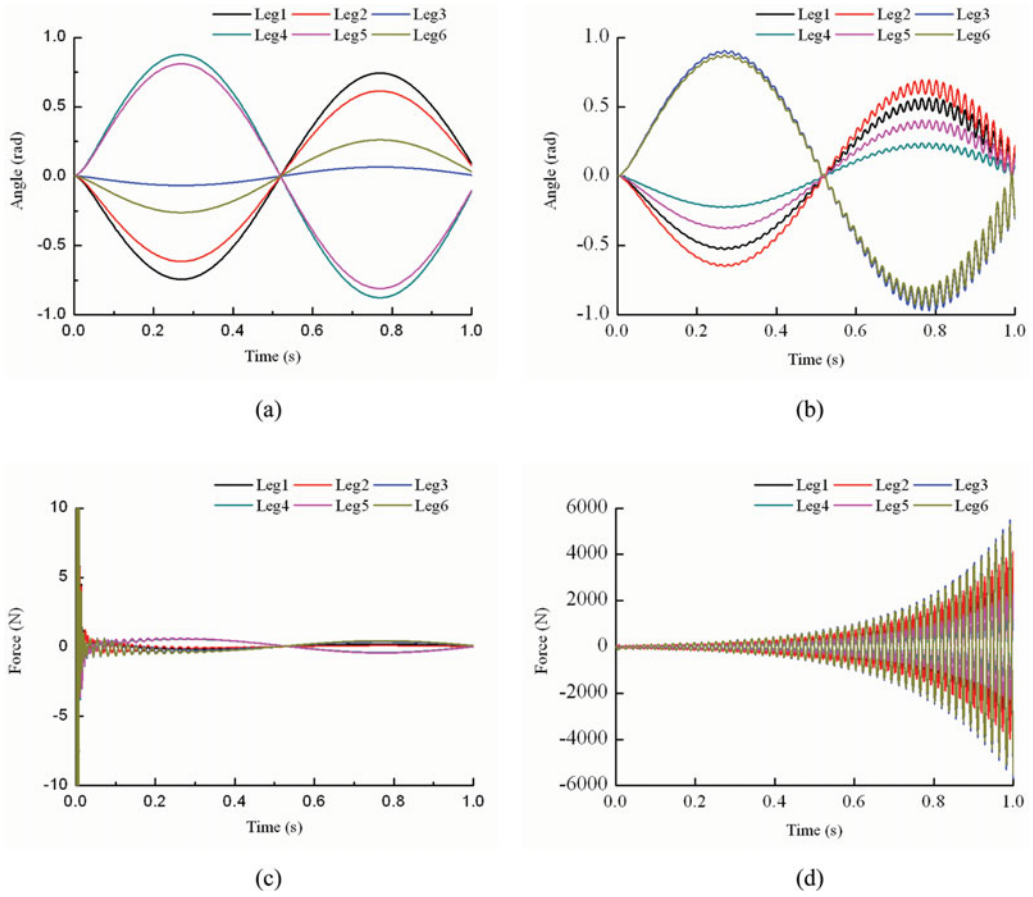


Fig. 8. Responses to eigenvalues: (a) Position tracking to the minimum eigenvalue; (b) position tracking to the maximum eigenvalue; (c) driving force to the minimum eigenvalue; (d) driving force to the maximum eigenvalue.

In a broad sense, if we denote the output torque of motors by $\mathbf{T}_r$, the ratio of the output torque to the acceleration of the motors is determined by

$$\frac{\|\mathbf{T}_r\|}{\|\ddot{\boldsymbol{\alpha}}\|} = \sqrt{\frac{\ddot{\boldsymbol{\alpha}}^T \left(\mathbf{I}^T\mathbf{I}\right) \ddot{\boldsymbol{\alpha}}}{\ddot{\boldsymbol{\alpha}}^T \ddot{\boldsymbol{\alpha}}}}. \tag{7}$$

This ratio describes how much output torque is produced by the given acceleration of motors. This relationship results in an eigenvalue problem of matrix $\mathbf{I}$; that is, if motor's acceleration is unity, the output torque is bounded within an ellipsoid expanded by the eigenvectors of matrix $\mathbf{I}$. The maximum output torque will be generated in the direction of eigenvector corresponding to maximum eigenvalue, and the ratio turns out to be the maximum eigenvalue. The result is in agreement with that illustrated in Fig. 8. Therefore, the maximum eigenvalue $\lambda_{\max}$ of the inertia matrix $\mathbf{I}$ is rationally defined as the inertia index of the Stewart platform.

4. Experiments

In this section, we describe experiments conducted to verify the theory proposed in this paper. Figure 9 illustrates the prototype of the experimental Stewart platform. The control system comprises an industrial PC, a motion control card (Delta Tau Turbo PMAC PCI), six AC servo drivers (Sinano H15C-CC201G38E), and six AC servomotors (Dongyuan TECO 6CC201G-3DEBEAS). A joint space PID controller is used in the experimental Stewart platform. The AC servo driver performs the current and speed loops, and the motion control card performs the position loop.

https://doi.org/10.1017/S0263574714002112 Published online by Cambridge University Press



Fig. 9. Experimental Stewart platform.

The parameters of the prototype are given in Appendix A. The coordinate system established is the same as in Section 2. Because the prototype is limited by its stiffness, movement of the platform under heavy load will result in the vibration of prototype. Parameters of PID controllers remain constant during the experiment. Only a small scale factor of the position loop can be selected in case of bloody strongly vibration of mechanical structure. Therefore, the dynamic performance of position tracking of the control system is not clear. By comparison, the vibration of mechanical structure is more obvious. Variation in the vibration results from the load inertia of the prototype. Therefore, the vibration of the mechanical structure reflects the degree of load inertia for a given motion. The force sensors mounted on the legs are applied to measure the vibration of the mechanical structure.

Similar to the description given in Section 3, the motors are desired to track sinusoidal signals with a frequency of 2π Hz and an amplitude of $\frac{\pi}{2}\mathbf{P}_i$ rad. The desired sinusoidal signals (frequency is 2π Hz) are sent to six motors. At a configuration of $[0,\ 0,\ -0.987\text{m},\ 0^\circ,\ 0^\circ,\ 0^\circ]^T$, the maximum and minimum eigenvalues, and their corresponding eigenvectors are calculated. Vibrations recorded by force sensors as minimum and maximum eigenvalues are shown in Fig. 10,

$$\lambda_1 = 0.50 \times 10^{-5}, \quad \mathbf{P}_1 = [-0.4118, -0.4678, -0.1445, 0.5269, 0.5563, -0.0591]^T,$$
$$\lambda_6 = 17.56 \times 10^{-5}, \quad \mathbf{P}_6 = [0.5045, -0.3612, -0.0091, 0.5707, -0.4954, -0.2095]^T.$$

At a configuration of $[0,0,\ -\ 0.987\text{m}, 10^\circ, 0^\circ, 0^\circ]^T$, the maximum and minimum eigenvalues, and their corresponding eigenvectors are calculated. Vibrations recorded by force sensors as minimum and maximum eigenvalues are shown in Fig. 11,

$$\lambda_1 = 0.50 \times 10^{-5}, \quad \mathbf{P}_1 = [-0.0253, 0.5929, 0.5930, -0.0252, -0.3844, -0.3844]^T,$$
$$\lambda_6 = 18.81 \times 10^{-5}, \quad \mathbf{P}_6 = [-0.5709, 0.2096, 0.2096, -0.5709, 0.3608, 0.3608]^T.$$

At a configuration of $[0,\ 0,\ -\ 1.037\text{m},\ 0^\circ,\ 0^\circ,\ 0^\circ]^T$, the maximum and minimum eigenvalues, and their corresponding eigenvectors are calculated. Vibrations recorded by force sensors as the minimum

https://doi.org/10.1017/S0263574714002112 Published online by Cambridge University Press

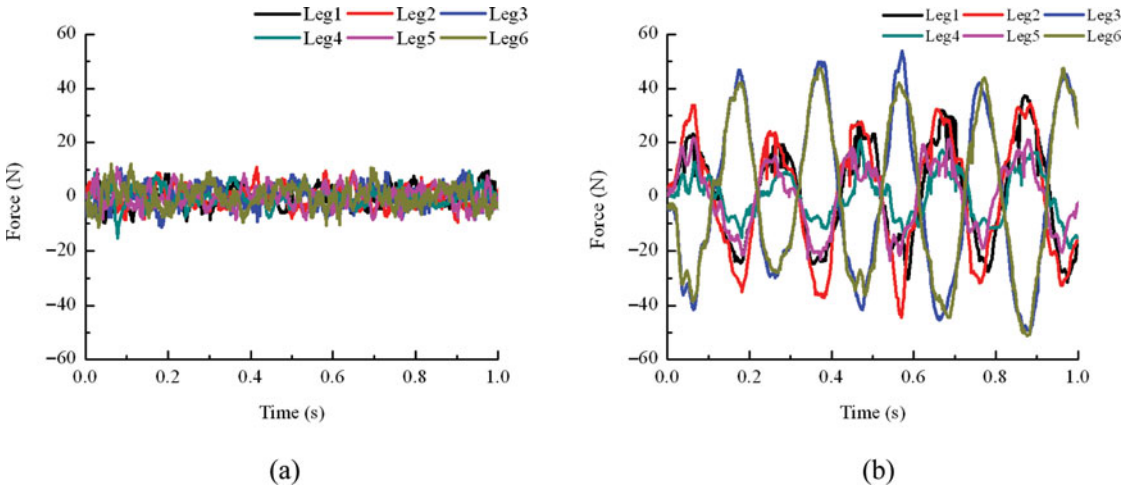


Fig. 10. Configuration of $Z = -0.987$ m: (a) minimum eigenvalue, and (b) maximum eigenvalue.

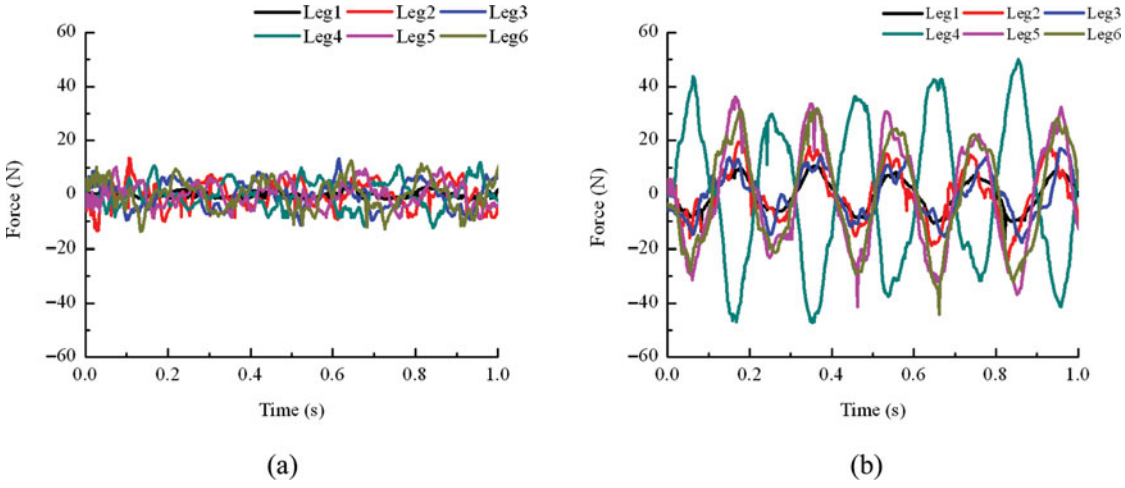


Fig. 11. Configuration of $A = 10^{\circ}$: (a) minimum eigenvalue, and (b) maximum eigenvalue.

and maximum eigenvalues are shown in Fig. 12,

$$\lambda_1 = 0.50 \times 10^{-5} \quad \mathbf{P}_1 = [-0.4774, -0.3943, -0.0425, 0.5624, 0.5199, -0.1681]^T,$$
$$\lambda_6 = 19.15 \times 10^{-5}, \quad \mathbf{P}_6 = [-0.3347, -0.4133, 0.5748, -0.1425, -0.2400, 0.5558]^T.$$

In Figs. 10(a), 11(a), and 12(a), the vibration magnitudes of force sensors vary within a narrow range because minimal output torque is generated at the acceleration of motors in the direction corresponding to the minimum eigenvalue, which represents the load inertia of the Stewart platform. In contrast, the vibration magnitudes shown in Figs. 10(b), 11(b), and 12(b) vary within a wide range. In this case, the Stewart platform possesses a load inertia equaling the maximum eigenvalue. Notably, the vibration magnitude in Fig. 12(b) is greater than that shown in Fig. 10(b). This result is reasonable because the maximum eigenvalue at the configuration of $Z = -1.037$ m is greater than that the configuration of $Z = -0.987$ m. The experimental results show that the eigenvalue characteristic of the inertia of the Stewart platform and the direction corresponding to the maximum eigenvalue will generate the maximum output torque. The forces in Fig. 12(b) are not in accordance with the driving forces in Fig. 8(d) for two reasons. A small scale factor of the position loop is selected in the experiment so that no high frequency vibration appears in position tracking. The force sensors in the experiment are influenced by the vibration of mechanical structure. The aforementioned experimental results mainly reflect the influence of inertia on the mechanical structure of the Stewart platform.

https://doi.org/10.1017/S0263574714002112 Published online by Cambridge University Press

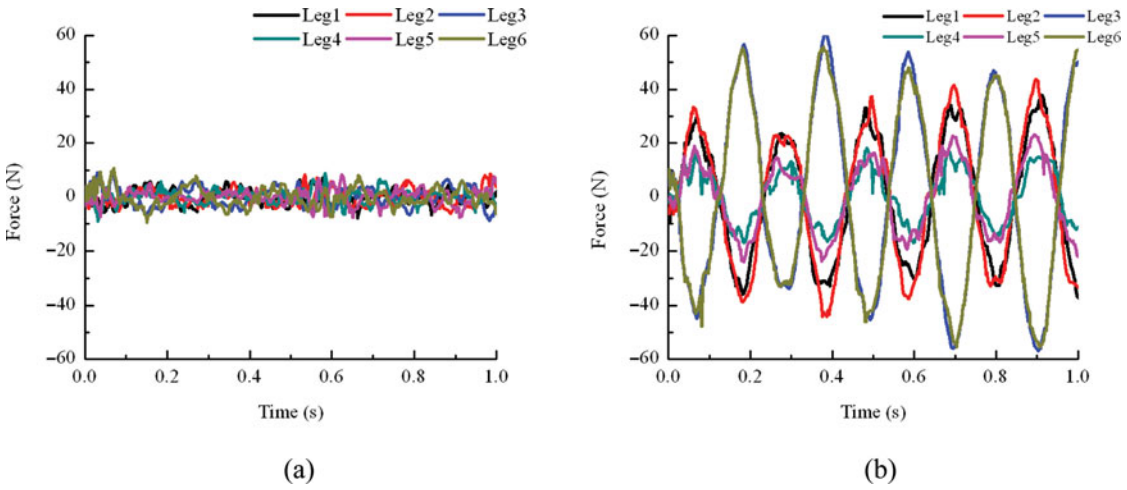


Fig. 12. Configuration of $Z = -1.037$ m: (a) minimum eigenvalue, and (b) maximum eigenvalue.

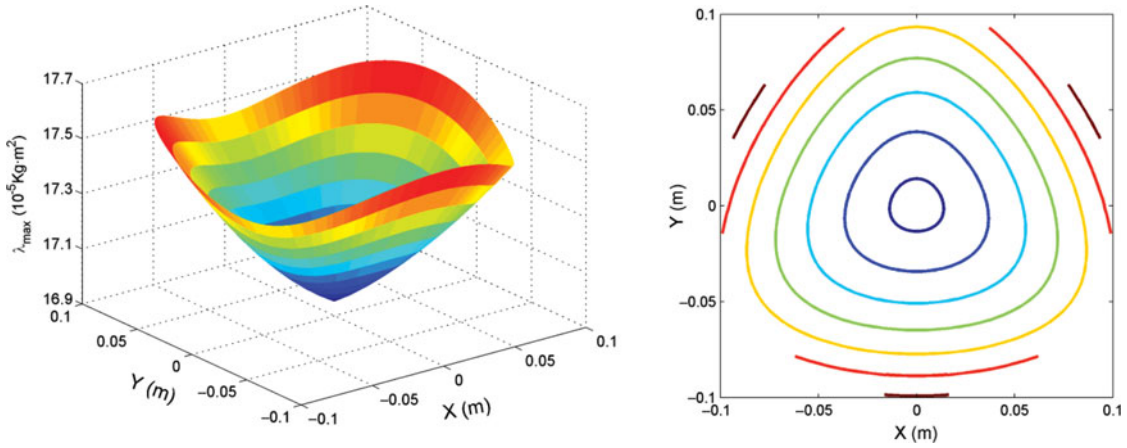


Fig. 13. Inertia index in the maximum horizontal plane.

5. Application

5.1. Inertia distribution

In parallel manipulators, the inertia matrix is configuration-dependent, leading to the configuration-dependent inertia index. In this section, the distribution of the inertia index in the operational workspace is provided. Parameters of the Stewart platform are given in Appendix A. The operational workspace is described as a sphere with a radius of 0.1 m and a center of (0, 0, −0.967 m). The orientation angles φ, θ, and ϕ in the sphere range from -10° to 10°.

The distribution of the inertia index in the maximum plane of operational workspace ($Z = -0.967$ m, $\varphi = \theta = \phi = 0^\circ$) is shown in Fig. 13. The inertia index is minimal in the center of the operational workspace and increases toward the edge of the platform. Because the mechanical structure is symmetrical about the center, the distribution of the inertia is also symmetrical. The inertia index ranges from 16.95×10^{-5} to 17.61×10^{-5}kg · m^2 and is relatively narrow. The distribution of the inertia index along the z-axis ($X = Y = 0$ m, $\varphi = \theta = \phi = 0^\circ$) is illustrated in Fig. 14. The value of inertia index increases with the distance of the platform from the base. The inertia index varies within relatively wide limits, from 14.11×10^{-5} to 20.14×10^{-5}kg · m^2. For the case where the platform is located at the center of the operational workspace ($X = Y = 0$ m, $Z = -0.967$ m), the relations between the inertia index and the rotation angles of the platform are illustrated in Fig. 15. The value of inertia index increases with rotation angles but does not change substantially; it ranges from 16.95×10^{-5} to 18.31×10^{-5}kg · m^2. From the above distribution situation, we deduce that the maximum inertia index in the operational workspace appears on the surface of the sphere with the

https://doi.org/10.1017/S0263574714002112 Published online by Cambridge University Press

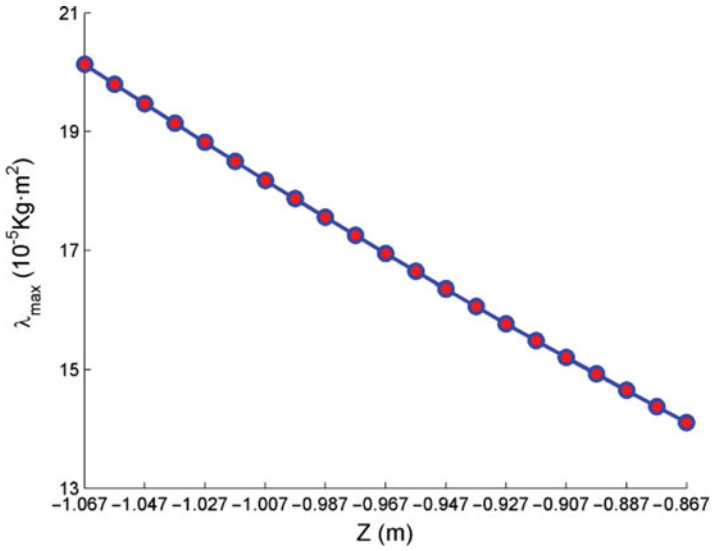


Fig. 14. Inertia index along the z-axis.

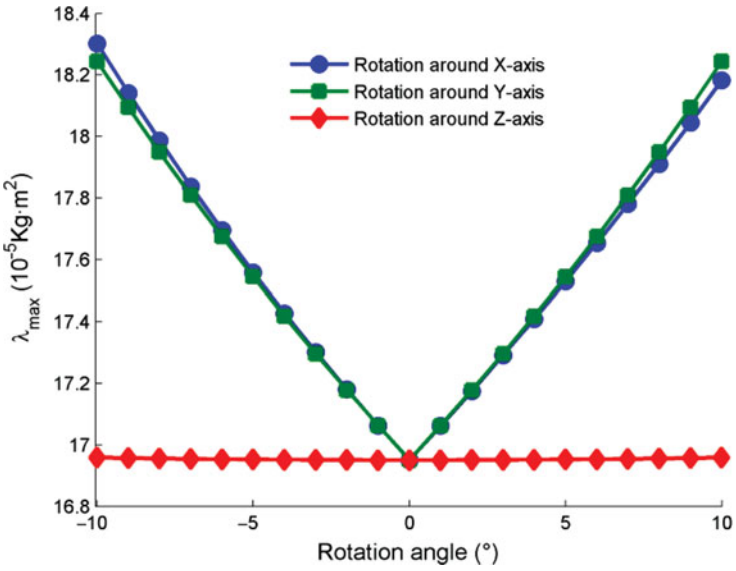


Fig. 15. Inertia indexes as functions of rotation angle.

orientation angles $\varphi = \theta = \phi = 10^\circ$, as shown in Fig. 16. The maximum value that the inertia index reaches is $22.39 \times 10^{-5}\text{kg} \cdot \text{m}^2$.

In the whole operational workspace, the inertia index of the Stewart platform ranges from 14.11×10^{-5} to $22.39 \times 10^{-5}\text{kg} \cdot \text{m}^2$. The inertia index greatly varies along the z-axis and appears to become quite large when the platform is situated far from the base. Therefore, for the sake of reducing the load inertia, the motion of the platform should be kept as close to the base as possible. According to the inertia matching principle proposed in our previous paper,[23] the available range of motor's inertia parameter is determined to be from 7.46×10^{-5} to $14.1 \times 10^{-5}\text{kg} \cdot \text{m}^2$.

5.2. Dimensional parameters

The inertia index is closely related to dimensional parameters. Four dimensional parameters will be analyzed: the radius of the universal joint r_B, the angle of the universal joints θ_B, the radius of the spherical joints r_M, and the angle of the spherical joint θ_M. The influence of dimensional parameters on the distribution of inertia index along the z-axis ($X = Y = 0$ m, $\varphi = \theta = \phi = 0^\circ$) is illustrated in Fig. 17.

https://doi.org/10.1017/S0263574714002112 Published online by Cambridge University Press

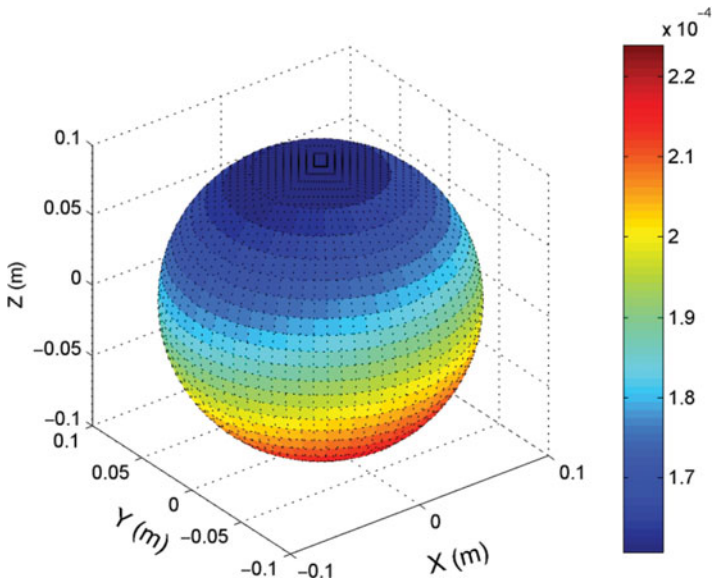


Fig. 16. Inertia index in the boundary of the operational workspace.

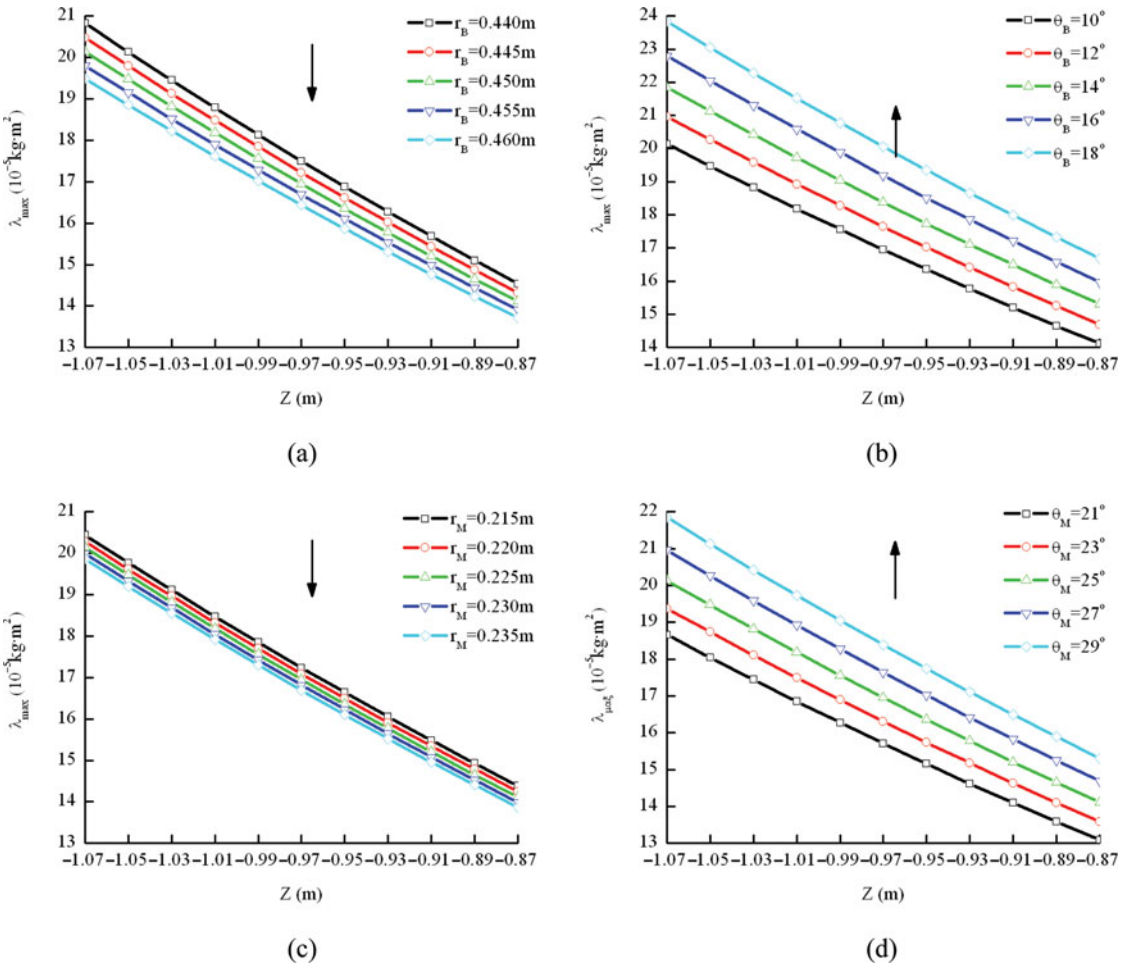


Fig. 17. Influence of dimensional parameters: (a) the radius of universal joints, (b) the angle of universal joints, (c) the radius of sphere joints, and (d) the angle of sphere joints.

https://doi.org/10.1017/S0263574714002112 Published online by Cambridge University Press

Table II. Dimensional parameters of the Stewart platform.

Physical meaning	Symbol	Value
Radius of spherical joints	r_M	0.225 m
Initial height of platform	h	0.250–0.350 m
Radius of universal joints	r_B	0.350–0.450 m
Angle of universal joints	θ_B	10° –60°
Angle of spherical joints	θ_M	15° –60°

As shown in Figs. 17(a) and (c), the inertia index value decreases with increase in the radius of joint points. In contrast, the inertia index value will decrease as the angle of joint points increases, as shown in Figs. 17(b) and (d). The inertia index greatly varies with the angle of joint points. In contrast, the radius of joint points has weaker influence on inertia index. Therefore, the angles of joint points are key elements in reducing the load inertia and should be designed as small as possible.

5.3. Dimensional optimization

As discussed in Section 5.2, dimensional parameters strongly influence the inertia. Obviously, the current dimensional parameters are not the optimal choice from the viewpoint of dynamics. In this section, dimensional optimization is implemented for the purpose of small inertia. As shown in Fig. 1, five dimensional parameters need to be determined: the radius of the universal joint, r_B, the angle of the universal joints, θ_B, the radius of the spherical joints, r_M, and the angle of the spherical joint, θ_M, and the initial height, h, between the universal and spherical joint points.

The condition number κ of the Jacobian matrix $\mathbf{H}^{-T}$ is often used to evaluate the kinematic isotropy and dexterity of a manipulator. The condition number should be restricted within certain limits to obtain good kinematic performance. In addition, the inertia index $\lambda_{\max}$ proposed in this paper has been demonstrated to be important in the evaluation of load inertia. The inertia index should be kept as small as possible to achieve good dynamic performance. To achieve the two design goals, the dimensional parameters can be optimized in the following manner.

Step 1: According to the requirement, the operational workspace is defined as a sphere with a radius of 0.1 m and the orientation angles φ, θ, and ϕ in the sphere range from -10° to 10°. The radius of spherical joints r_M is determined by the end-effector mounted on it. The others need to be optimized in the following. As illustrated in Fig. 14, the initial height h should be kept small to attain better dynamic performance. An increase in the radius of universal joints r_B decreases the inertia index, as shown in Fig. 17(a); however, this increase in radius will also lengthen the legs. The angles of joints θ_B and θ_M should be sufficiently large to accommodate the installation of universal and spherical joints. As mentioned previously, the determined value ranges of the parameters are listed in Table II.

Step 2: Optimization is to minimize the objective function $f_1 = \max\{\kappa(r_B, \theta_B, \theta_M)\}$ when $(r_B, \theta_B, \theta_M) \in \Omega$, where f_1 is the maximum condition number of the Stewart platform in the operational workspace, and Ω is the value range of dimensional parameters. The optimization can be solved by the MATLAB routine "fmincon." The optimization result is $h = 0.344$ m, $r_B = 0.424$m, $\theta_B = 10.06^\circ$, and $\theta_M = 15.07^\circ$, and the minimum objective function $\kappa_{\min}$ is 2.2285. For this group of dimensional parameters, the distribution of the condition number and the inertia index on the boundary of operational workspace ($\varphi = \theta = \phi = 10^\circ$) is depicted in Fig. 18. The maximum condition number and inertia index are 2.2285 and 7.99×10^{-5}kg $\cdot$ m^2, respectively.

Step 3: Optimization is to minimize the objective function $f_2 = \max\{\lambda_{\max}(r_B, \theta_B, \theta_M)\}$ when $(r_B, \theta_B, \theta_M) \in \Omega$ and $\kappa \leq 1.25\kappa_{\min}$, where f_2 is the maximum inertia index of the Stewart platform in the operational workspace, Ω is the value range of dimensional parameters, and κ is the maximum condition number of the Stewart platform in operational workspace. The purpose of the constraint $\kappa \leq 1.25\kappa_{\min}$ is to obtain a small inertia index at the expense of condition number. The optimization result is $h = 0.322$ m, $r_B = 0.376$ m, $\theta_B = 10.00^\circ$, and $\theta_M = 15.00^\circ$. The distribution of the condition number and inertia index on the boundary of operational workspace ($\varphi = \theta = \phi = 10^\circ$) is depicted in Fig. 19. The maximum condition number and inertia index are 2.3078 and 7.76×10^{-5} kg$\cdot$m^{2}respectively. In comparison with Fig. 18, the inertia index is future reduced because of

https://doi.org/10.1017/S0263574714002112 Published online by Cambridge University Press

Table III. Optimized dimensional parameters of the Stewart platform.

Physical meaning	Symbol	Value
Radius of spherical joints	r_M	0.225 m
Initial height of platform	h	0.322 m
Radius of universal joints	r_B	0.376 m
Angle of universal joints	θ_B	10°
Angle of spherical joints	θ_M	15°

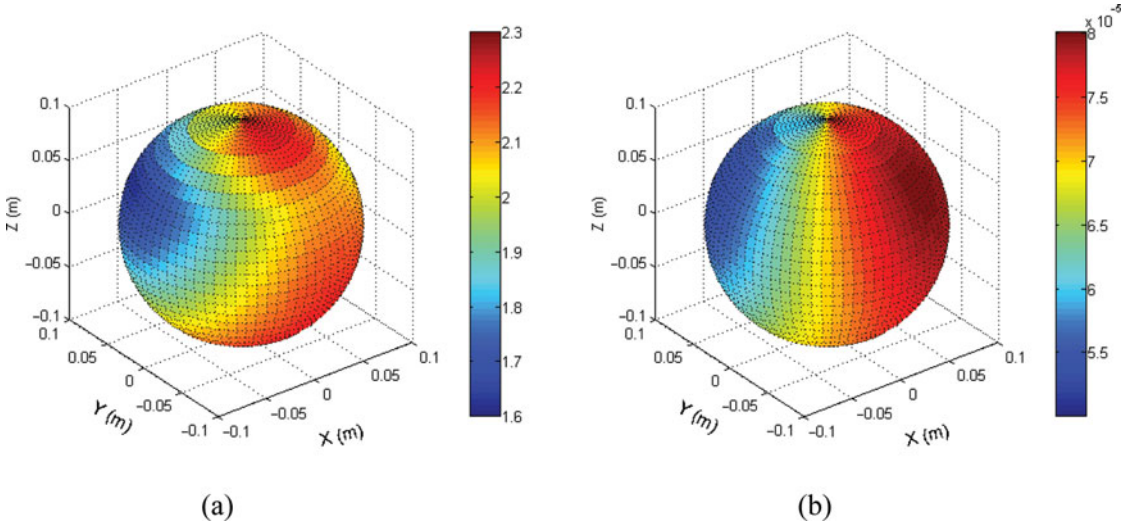


Fig. 18. Distribution in the operational workspace: (a) condition number, and (b) inertia index.

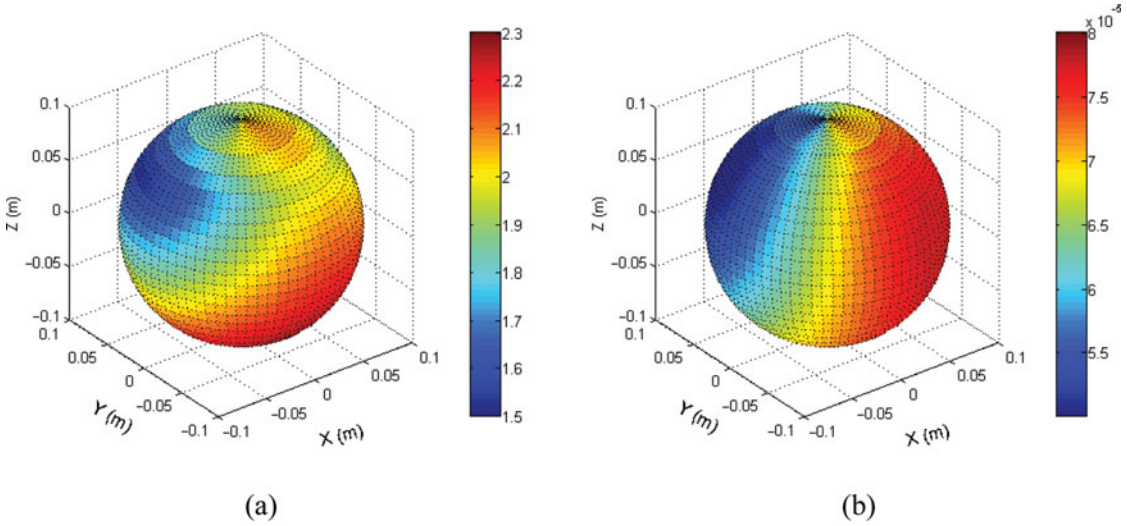


Fig. 19. Distribution in the operational workspace: (a) condition number, and (b) inertia index.

the concession in condition number. In this way, the demands of both condition number and inertia index of the Stewart platform can be satisfied.

According to the above optimization steps, the final optimized dimensional parameters are listed in Table III. In order to verify the optimization, we conduct simulation to compare the dynamic response of the Stewart platform with original and optimized parameters. Similar to the simulation in Section 2, the motors are desired to track sinusoidal signals. Figure 20 shows the responses of motors to maximum eigenvalues of original and optimized parameters when the platform locates at the center of its operational workspace. It can be seen from Fig. 20 that there is a great improvement in the

https://doi.org/10.1017/S0263574714002112 Published online by Cambridge University Press

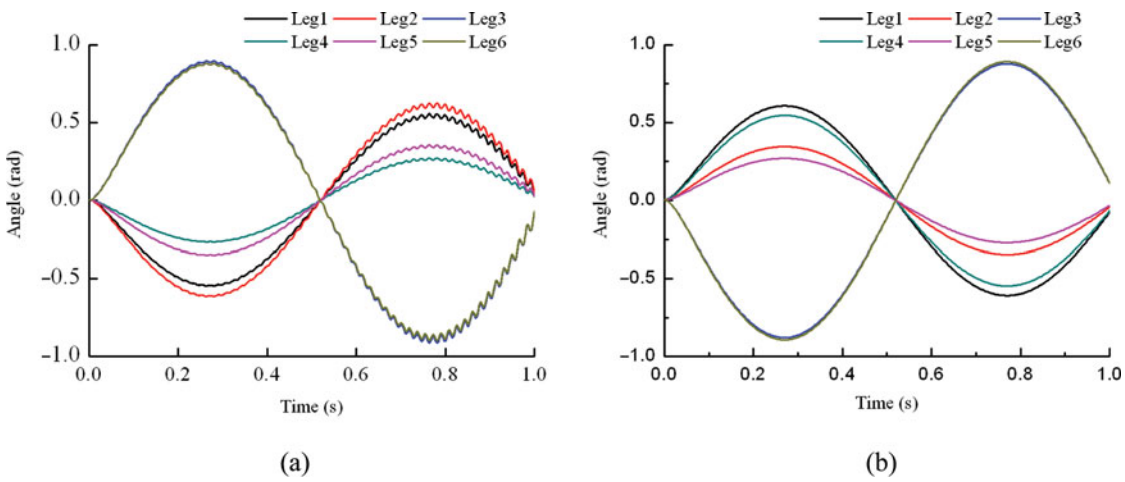


Fig. 20. Responses to maximum eigenvalues: (a) the original parameters, (b) the optimal parameters.

dynamic response of motors. The results clearly illustrate that the above dimensional optimization based on the proposed inertia index can effectively reduce the load inertia of the Stewart platform.

6. Conclusions

The essential characteristic of inertia of the Stewart platform is coupled. However, the load inertia converted to the driving motors of the Stewart platform can be decoupled according to the analysis in the present paper. Independent control channels are determined on the basis of the decoupling of inertia of the Stewart platform. The Adams simulation is performed to show that eigenvalues of inertia matrix represent the load inertia of control channels. The eigenvalue characteristic of inertia of the Stewart platform is further verified through experiments. Therefore, the maximum eigenvalue of inertia matrix is put forward as inertia index. The proposed inertia index is devoted to dimensional optimization of the Stewart platform, and a set of optimized dimensions are obtained that provide good dynamic performance.

Acknowledgements

This research is sponsored by the National Natural Science Foundation of China (Nos. 11178012, 51205224) and the National Natural Science Funds for Distinguished Young Scholars of China (No. 51225503).

References

1. Y. Cao, C. Gosselin, P. Ren and H. Zhou, "Orientation ability analyses of a special class of the Stewart-Gough parallel manipulators using the unit quaternion representation," *Adv. Robot.* **27**(2), 147–158 (2013).
2. D. Wang, R. Fan and W. Chen, "Performance enhancement of a three-degree-of-freedom parallel tool head via actuation redundancy," *Mech. Mach. Theory* **71**, 142–162 (2014).
3. F. Xie, X. J. Liu, Z. You and J. Wang, "Type synthesis of 2T1R-type parallel kinematic mechanisms and the application in manufacturing," *Robot. Comput. Integr. Manuf.* **30**(1), 1–10 (2014).
4. X. Tang, W. Zhu, C. Sun and R. Yao, "Similarity model of feed support system for FAST," *Exp. Astron.* **29**(3), 177–187 (2011).
5. Z. F. Shao, X. Tang, X. Chen and L. P. Wang, "Driving force analysis for the secondary adjustable system in FAST," *Robotica* **29**(6), 903–915 (2011).
6. D. Yu, H. Li and W. Chen, "Kinematic calibration of parallel robots for docking mechanism motion simulation," *Int. J. Adv. Robot. Syst.* **8**(4), 158–165 (2011).
7. H. Xiong, Q. Huang, J. Ma and J. Han, "Research on Co-Modeling Virtual Prototype of Motion System of Flight Simulator," *Proceedings of IEEE International Conference on Mechatronics and Automation, 2009 (ICMA 2009)* (IEEE, Washington, DC, 2009, Aug.) pp. 2260–2264.

https://doi.org/10.1017/S0263574714002112 Published online by Cambridge University Press

8. B. Dasgupta and T. S. Mruthyunjaya, "Closed-form dynamic equations of the general Stewart platform through the Newton–Euler approach," *Mech. Mach. Theory* **33**(7), 993–1012 (1998).
9. H. Abdellatif and B. Heimann, "Computational efficient inverse dynamics of 6-DOF fully parallel manipulators by using the Lagrangian formalism," *Mech. Mach. Theory* **44**(1), 192–207 (2009).
10. L. W. Tsai, "Solving the inverse dynamics of a Stewart–Gough manipulator by the principle of virtual work," *J. Mech. Des.* **122**, 3 (2000).
11. Y. Yun and Y Li. "Multi-Degree of Freedom Vibration Model for a 3-DOF Hybrid Robot," *Proceedings of the IEEE/ASME International Conference on Advanced Intelligent Mechatronics, 2009 (AIM 2009)* (IEEE, Washington, DC, 2009, Jul.) pp. 1474–1479.
12. A. M. Lopes, "Complete dynamic modelling of a moving base 6-dof parallel manipulator," *Robotica* **28**(5), 781–793 (2010).
13. Y. Ting, Y. S. Chen and S. M. Wang, "Task-Space Control Algorithm for Stewart Platform," *Proceedings of the 38th IEEE Conference on Decision and Control*, vol. 4 (IEEE, Washington, DC, 1999) pp. 3857–3862.
14. W. Shang, S. Cong and Y. Ge, "Coordination motion control in the task space for parallel manipulators with actuation redundancy," *IEEE Trans. Autom. Sci. Eng.* **10**(3), 665–673 (2013).
15. C. Yang, Q. Huang, H. Jiang, O. Ogbobe Peter and J. Han, "PD control with gravity compensation for hydraulic 6-DOF parallel manipulator," *Mech. Mach. Theory* **45**(4), 666–677 (2010).
16. D. H. Kim, J. Y. Kang and K. I. Lee, "Robust tracking control design for a 6-DOF parallel manipulator," *J. Robot. Syst.* **17**(10), 527–547 (2000).
17. Y. X. Su, B. Y. Duan and C. H. Zheng, "Nonlinear PID control of a six-DOF parallel manipulator," *IEEE Proc.,Control Theory Appl.* **151**(1), 95–102 (2004).
18. X. Jian, T. Zhiyong, P. Zhongcai, H. Shao and L. Lanbo, "Adaptive controller for 6-DOF parallel robot using TS fuzzy inference," *Int. J. Adv. Robot. Syst.* **10**, 1–9 (2013).
19. Y. Liu, X. Jia, J. Han and X. Zhao, "A Robust Adaptive Fuzzy Sliding Mode Control Method of 3-RRRT Parallel Manipulator," *Proceedings of the IEEE International Conference on Automation and Logistics, 2009 (ICAL '09)* (IEEE, Washington, DC, 2009, Aug.) pp. 1883–1887.
20. T. Huang, J. Mei, Z. Li, X. Zhao and D. G. Chetwynd, "A method for estimating servomotor parameters of a parallel robot for rapid pick-and-place operations," *J. Mech. Des.* **127**, 596–601 (2005).
21. Y. Chen and J. E. McInroy, "Decoupled control of flexure-jointed hexapods using estimated joint-space mass-inertia matrix," *IEEE Trans. Control Syst. Technol.* **12**(3), 413–421 (2004).
22. Z. Shao, X. Tang, X. Chen and L. Wang, "Inertia matching of a 3-RRR reconfigurable planar parallel manipulator," *Chin. J. Mech. Eng.* **22**(6), 791–799 (2009).
23. Z. Shao, X. Tang, X. Chen and L. Wang, "Research on the inertia matching of the Stewart parallel manipulator," *Robot. Comput.-Integr. Manuf.* **28**(6), 649–659 (2012).
24. P. Ogbobe, Y. Zhengmao, J. Hougzhou and H. Junwei, "Analytical Formulation of Coupling Effects Matrix Between Degrees of Freedom Motion of Parallel Robots," *Proceedings of the IEEE International Conference on Intelligent Computation Technology and Automation (ICICTA 2010)*, vol. 1 (2010, May), pp. 711–714.
25. Y. Yao, S. Fu and L. Han, "Block diagonal dominance analysis and judgment of Stewart platform's joint-space inertia matrix," *Chin. J. Mech. Eng.* **44** (6), 101–106 (2008).

Appendix A: Parameters of the Stewart platform

All the parameters in Appendix A are default in SI units.

Orientation of the platform based on the Roll-Pitch-Yaw (RPY) Euler angle convention in $\{B\}$:

$$\begin{aligned}\Re &= \Re(z,\phi)\cdot\Re(y,\theta)\cdot\Re(x,\varphi)\\ &= \begin{bmatrix} \cos\phi\cos\theta & \cos\phi\sin\theta\sin\varphi-\sin\phi\cos\varphi & \cos\phi\sin\theta\cos\varphi+\sin\phi\sin\varphi\\ \sin\phi\cos\theta & \sin\phi\sin\theta\sin\varphi+\cos\phi\cos\varphi & \sin\phi\sin\theta\cos\varphi-\cos\phi\sin\varphi\\ -\sin\theta & \cos\theta\sin\varphi & \cos\theta\cos\varphi \end{bmatrix}.\end{aligned}$$

Universal joints described in $\{B\}$:

$$[\mathbf{b}_1,\mathbf{b}_2,\mathbf{b}_3,\mathbf{b}_4,\mathbf{b}_5,\mathbf{b}_6] = \begin{bmatrix} 0.4078 & 0.3686 & -0.3686 & -0.4078 & -0.0392 & 0.0392\\ 0.1902 & 0.2581 & 0.2581 & 0.1902 & -0.4483 & -0.4483\\ -0.039 & -0.039 & -0.039 & -0.039 & -0.039 & -0.039 \end{bmatrix}.$$

https://doi.org/10.1017/S0263574714002112 Published online by Cambridge University Press

Sphere joints described in $\{P\}$:

$$[\mathbf{p}_1, \mathbf{p}_2, \mathbf{p}_3, \mathbf{p}_4, \mathbf{p}_5, \mathbf{p}_6] = \begin{bmatrix} 0.2146 & 0.0487 & -0.0487 & -0.2146 & -0.1659 & 0.1659 \\ 0.0677 & 0.2197 & 0.2197 & 0.0677 & -0.1520 & -0.1520 \\ 0.016 & 0.016 & 0.016 & 0.016 & 0.016 & 0.016 \end{bmatrix}.$$

Mass, position vector of mass center, and moment of inertia of the upper part of the leg:

$$m_L = 7.4697, \quad r_L = \begin{bmatrix} 0.25377559 & 0.00023425 & 0.00050927 \end{bmatrix}^T,$$

$$I_L = \begin{bmatrix} 0.00754409 & -0.00007554 & 0.00568917 \\ -0.00007554 & 0.21747869 & 0.00000304 \\ 0.00568917 & 0.00000304 & 0.21670684 \end{bmatrix}.$$

Mass, position vector of mass center, and moment of inertia of the lower part of the leg:

$$m_U = 3.3546, \quad r_U = \begin{bmatrix} -0.27523968 & 0.000055 & -0.00074736 \end{bmatrix}^T,$$

$$I_U = \begin{bmatrix} 0.00107594 & 0.00005513 & 0.00010620 \\ 0.00005513 & 0.14460083 & -0.00000599 \\ 0.00010620 & -0.0000599 & 0.14442262 \end{bmatrix}.$$

Mass, position vector of mass center, and moment of inertia of the platform:

$$m_P = 55.5319, \quad r_P = \begin{bmatrix} 0.00000000 & 0.00000000 & 0.12226763 \end{bmatrix}^T,$$

$$I_P = \begin{bmatrix} 0.53425303 & 0 & 0 \\ 0 & 0.53425303 & 0 \\ 0 & 0 & 0.35160382 \end{bmatrix}.$$

https://doi.org/10.1017/S0263574714002112 Published online by Cambridge University Press